

| REPORT DOCUMENTATION PAGE | | | | Form Approved OMB No. 0704-0188 | |
|---|--------------|-----------------------------------|-------------------------------|---|---|
| Public reporting burden for this collection of information is estimated to average 1 hour per response, including the time for reviewing instructions, searching existing data sources, gathering and maintaining the data needed, and completing and reviewing this collection of information. Send comments regarding this burden estimate or any other aspect of this collection of information, including suggestions for reducing this burden to Department of Defense, Washington Headquarters Services, Directorate for Information Operations and Reports (0704-0188), 1215 Jefferson Davis Highway, Suite 1204, Arlington, VA 22202-4302. Respondents should be aware that notwithstanding any other provision of law, no person shall be subject to any penalty for failing to comply with a collection of information if it does not display a currently valid OMB control number. PLEASE DO NOT RETURN YOUR FORM TO THE ABOVE ADDRESS. | | | | | |
| 1. REPORT DATE (DD-MM-YYYY) 04-04-2011 | | 2. REPORT TYPE Journal Article | | 3. DATES COVERED (From - To) | |
| 4. TITLE AND SUBTITLE Insight into Hydrazinium Nitrates, Azides, Dicyanamide, and 5-Azidotetrazolate Ionic Materials from Simulations and Experiments | | | | 5a. CONTRACT NUMBER | |
| | | | | 5b. GRANT NUMBER | |
| | | | | 5c. PROGRAM ELEMENT NUMBER | |
| 6. AUTHOR(S) Justin B. Hooper, Oleg Borodin, Stefan Schneider | | | | 5d. PROJECT NUMBER | |
| | | | | | |
| | | | | 5f. WORK UNIT NUMBER 23030423 | |
| 7. PERFORMING ORGANIZATION NAME(S) AND ADDRESS(ES) Wasatch Molecular, Inc. 2141 St. Marys Dr., Ste 102 Salt Lake City, UT 84108 | | | | 8. PERFORMING ORGANIZATION REPORT NUMBER AFRL-RZ-ED-JA-2011-119 | |
| 9. SPONSORING / MONITORING AGENCY NAME(S) AND ADDRESS(ES) Air Force Research Laboratory (AFMC) AFRL/RZS 5 Pollux Drive Edwards AFB CA 93524-7048 | | | | 10. SPONSOR/MONITOR'S ACRONYM(S) | |
| | | | | 11. SPONSOR/MONITOR'S NUMBER(S) AFRL-RZ-ED-JA-2011-119 | |
| 12. DISTRIBUTION / AVAILABILITY STATEMENT Approved for public release; distribution unlimited (PA #10996). | | | | | |
| 13. SUPPLEMENTARY NOTES For publication in the Journal of Physical Chemistry B. | | | | | |
| 14. ABSTRACT A transferrable, polarizable quantum chemistry-based force field has been developed for hydrazinium, monomethylhydrazinium, and dimethylhydrazinium cations in combination with the nitrate, azide, dicyanamide, and 5-azidotetrazolate anions. Quantum chemistry calculations were performed on the neutral precursors, ions and cation-anion complexes employing aug-ccpVDz (cc-pVTz) basis functions at MP2 level or in conjunction with M05-2X density functional. Inclusion of a lone-pair on hydrazinium-based cations significantly improved ion electrostatic description and prediction of the crystal structure in molecular dynamics (MD). Seven different ionic systems have been investigated: [N ₂ H ₅][NO ₃], [(CH ₃)N ₂ H ₄][NO ₃], [(CH ₃) ₂ N ₂ H ₃][NO ₃], [N ₂ H ₅][CN ₇], [(CH ₃)N ₂ H ₄][N ₃], [(CH ₃) ₂ N ₂ H ₃][N ₃], [N ₂ H ₅][N(CN) ₂]. For all but the [(CH ₃) ₂ N ₂ H ₃][NO ₃] and [N ₂ H ₅][N(CN) ₂], QC calculations of a single, gas phase ion pair predicts spontaneous deprotonation of the cation. Crystal lattice parameters obtained from MD simulations were compared with experiments for ionic crystals of these seven systems, with the experimentally determined crystal structure of [N ₂ H ₅][N(CN) ₂] also presented here, enabling comparison of simulation and experiment for that compound. In general, MD simulations predicted crystal lattice vectors/angles (volumes) within a 5% (3%) absolute margin of error from experiments, with outlying values of 5-6.6 % for three crystals [(CH ₃)N ₂ H ₄][N ₃], [N ₂ H ₅][NO ₃], [(CH ₃)N ₂ H ₄][NO ₃] with combinations of particularly small anions and/or cations. Structural comparisons between ionic materials in the liquid and crystalline state are made, including the observation of two crystalline systems where the crystalline state induces conformational changes in the methylated hydrazinium cations compared to the gas phase and liquid states. The matrices of elastic constants were extracted from MD simulations for all seven ionic crystals and correlated with the structural motifs of ion interactions. | | | | | |
| 15. SUBJECT TERMS | | | | | |
| 16. SECURITY CLASSIFICATION OF: | | | 17. LIMITATION OF ABSTRACT | 18. NUMBER OF PAGES | 19a. NAME OF RESPONSIBLE PERSON |
| a. REPORT | b. ABSTRACT | c. THIS PAGE | | | Dr. Stefan Schneider |
| Unclassified | Unclassified | Unclassified | SAR | 52 | 19b. TELEPHONE NUMBER (include area code) N/A |

Insight into Hydrazinium Nitrates, Azides, Dicyanamide, and 5-Azidotetrazolate Ionic Materials from Simulations and Experiments

Justin B. Hooper,¹ Oleg Borodin^{1,2}, Stefan Schneider³

1. Wasatch Molecular Inc. 2141 St. Marys Dr., Ste 102, Salt Lake City, UT 84108
2. Department of Materials Science and Engineering, University of Utah, Salt Lake City, UT 84112
3. Air Force Research Laboratory, 10 East Saturn Blvd., Bldg. 8451, Edwards AFB, CA 93524

Abstract

A transferrable, polarizable quantum chemistry-based force field has been developed for hydrazinium, monomethylhydrazinium, and dimethylhydrazinium cations in combination with the nitrate, azide, dicyanamide, and 5-azidotetrazolate anions. Quantum chemistry calculations were performed on the neutral precursors, ions and cation-anion complexes employing aug-cc-pvDz (cc-pvTz) basis functions at MP2 level or in conjunction with M05-2X density functional. Inclusion of a lone-pair on hydrazinium-based cations significantly improved ion electrostatic description and prediction of the crystal structure in molecular dynamics (MD). Seven different ionic systems have been investigated: $[\text{N}_2\text{H}_5][\text{NO}_3]$, $[(\text{CH}_3)\text{N}_2\text{H}_4][\text{NO}_3]$, $[(\text{CH}_3)_2\text{N}_2\text{H}_3][\text{NO}_3]$, $[\text{N}_2\text{H}_5][\text{CN}_7]$, $[(\text{CH}_3)\text{N}_2\text{H}_4][\text{N}_3]$, $[(\text{CH}_3)_2\text{N}_2\text{H}_3][\text{N}_3]$, $[\text{N}_2\text{H}_5][\text{N}(\text{CN})_2]$. For all but the $[(\text{CH}_3)_2\text{N}_2\text{H}_3][\text{NO}_3]$ and $[\text{N}_2\text{H}_5][\text{N}(\text{CN})_2]$, QC calculations of a single, gas phase ion pair predicts spontaneous deprotonation of the cation.

Crystal lattice parameters obtained from MD simulations were compared with experiments for ionic crystals of these seven systems, with the experimentally determined crystal structure of $[\text{N}_2\text{H}_5][\text{N}(\text{CN})_2]$ also presented here, enabling comparison of simulation and experiment for that compound. In general, MD simulations predicted crystal lattice vectors/angles (volumes) within a 5% (3%) absolute margin of error from experiments, with outlying values of 5-6.6 % for three

crystals $[(\text{CH}_3)_2\text{N}_2\text{H}_4][\text{N}_3]$, $[\text{N}_2\text{H}_5][\text{NO}_3]$, $[(\text{CH}_3)_2\text{N}_2\text{H}_4][\text{NO}_3]$ with combinations of particularly small anions and/or cations. Structural comparisons between ionic materials in the liquid and crystalline state are made, including the observation of two crystalline systems where the crystalline state induces conformational changes in the methylated hydrazinium cations compared to the gas phase and liquid states. The matrices of elastic constants were extracted from MD simulations for all seven ionic crystals and correlated with the structural motifs of ion interactions in the crystals.

Introduction

Hydrazine, mixtures of hydrazine, or derivatives of hydrazine have been utilized for wide-ranging applications including polymer synthesis and processing, metal recovery and removal, pharmaceutical and agricultural applications, and bio-active applications such as herbicides and pesticides.¹ Perhaps the highest profile use for the hydrazine-based compounds, however, is provided by its longstanding role as a primary constituent of fuel systems for aerospace applications. Much research has been performed to elucidate the behavior of hydrazine and its methylated derivatives, monomethylhydrazine (MMH) and unsymmetric dimethylhydrazine (UDMH) by NASA^{2,3} and others in order to understand and control the conversion of these high energy chemicals into utilizable energy sources for aerospace applications. Unfortunately, the properties that make hydrazine and derivatives desirable compounds for these applications (namely high energy density, low reaction threshold, and high volatility associated with the liquid state) also contribute to its potential for harm during uncontrolled release. Hydrazine, MMH, and UDMH have been shown to be carcinogenic^{4,5} in laboratory tests involving rodents, and are suspected to have similar effects on humans via oral or vapor exposure.

Recently, ionic liquids (ILs) have attracted significant attention as solvent replacements^{6,7} and alternatives to the hydrazine-based hypergolic propellant.⁸⁻¹¹ Due to their ionic nature, IL vapor

pressure is low, resulting in a reduced environmental impact. Moreover, existence of numerous cation-anion combinations provides an avenue for optimization of the thermodynamic properties and reaction pathways. Experimental synthesis and characterization of novel high nitrogen containing ionic liquids and crystals have been hindered by reactivity, adding to the challenges and safety risk for experimental investigation. In cases such as these, the ability to accurately predict/describe thermodynamic response of these compounds without the associated risks of experimental measurements is of obvious utility. While there are many important properties that simulations have difficulty addressing, thermodynamic behavior of the material can be quantitatively described given an accurate force field description and proper simulation methodology. We have recently demonstrated the ability of our force field development and simulation process to provide simulation models that can accurately reproduce and predict density, heat of vaporization, ion diffusion coefficient, conductivity and viscosity of a diverse class of ionic liquids.¹² The same force field accurately predicted ionic crystal lattice parameters for four ionic crystals¹² as well as prediction of lattice parameters, conductivity, and melting point of a plastic crystalline system.¹³ Recently, however, Maginn's group has shown¹⁴ that it is quite difficult to achieve an accurate and consistent description of the modified hydrazinium nitrate ionic crystals. In this work, we undertake the challenge of developing a systematic force field that will describe crystal structures for these modified hydrazinium nitrate ionic materials. Furthermore, the developed polarizable force field will be extended to other anions such as azide (N_3^-), dicyanamide ($\text{N}(\text{CN})_2^-$) and 5-Azidotetrazolate (CN_7^-) in addition to NO_3^- and will be validated using seven high nitrogen content ionic crystals. After force field validation, we use MD simulations employing the developed force field to perform initial investigations of the mechanical properties in the crystalline system and investigate the structural interactions of cations and anions in the crystalline (and in some cases liquid) state, focusing on the differences of ion packing in the crystalline and liquid states.

The primary difficulty of developing a force field for the high nitrogen content ionic liquids and crystals is a lack of thermodynamic information in the liquid phase, which is often unstable for hydrazinium-based ionic liquids. Therefore, we rely heavily on the crystal structures of the hydrazinium-based ionic crystals for force field validation. Starting from a description of the neutral hydrazines as a baseline, we refine our force field models to produce the best *overall* description over the entirety of the crystal structures utilizing a single, consistent force field, with the idea that utilizing a consistent set of potential interactions for a number of ionic crystals with different crystal symmetries, melting temperatures, and anions will provide sufficient statistical variance over the specific sampled interactions of the hydrazinium-based ions to allow a good parameterization of a hydrazinium force field for use in the generic case.

To this end, we have investigated three substituted forms of hydrazine, in both their neutral and singly charged cationic states: Hydrazine and its cation (hydrazinium, N_2H_5^+), monomethylhydrazine (MMH) and its cation (methyl hydrazinium, $(\text{CH}_3)\text{N}_2\text{H}_4^+$), and the unsymmetric dimethylhydrazine (UDMH) and its cation (1,1-N-Dimethylhydrazinium, $(\text{CH}_3)_2\text{N}_2\text{H}_3^+$). Representations of the individual neutral molecules are presented as Figure 1A, while the cationic forms are presented as Figure 1B. In the case of the cationic forms, we have investigated a number of ionic crystals which utilize four common, singly charged nitrogen containing anions: Nitrate (NO_3^-), azide (N_3^-), dicyanamide ($\text{N}(\text{CN})_2^-$) and 5-Azidotetrazolate (CN_7^-), shown in Figure 1C. Note, that the CN_7^- anion has one of the highest known nitrogen content and was only recently characterized in detail.¹⁵ For the NO_3^- anion, crystals with all three cationic hydrazinium forms were available and will be utilized for the force field validation, while both the $\text{N}(\text{CN})_2^-$ and CN_7^- anion were investigated with only the N_2H_5^+ cation. For N_3^- , only crystal structures involving the methylated cations ($(\text{CH}_3)\text{N}_2\text{H}_4^+$ and $(\text{CH}_3)_2\text{N}_2\text{H}_3^+$) were available.^{16,17} For the $[\text{N}_2\text{H}_5][\text{N}(\text{CN})_2]$ system, X-Ray diffraction analysis has been performed to determine the crystal structure and allow for simulation comparison. The pertinent experimental

details for the determination of the crystal structure are presented in the supplemental information for this paper, while the crystal structure itself is available through the Cambridge Crystallographic Data Center (CCDC) as structure **XXXXXX**.

The remainder of the paper is organized as follows: In Section II the force field development is outlined, while in Section III we discuss simulation methodology. Section IV presents the results, while interpretation and directions for future work are provided in section V.

II. Force Field Development

Force Field Functional Form. The following form of the force field relating the potential energy $U^{Tot}(\mathbf{r})$ to atomic coordinates \mathbf{r} for the ensemble of atoms has been chosen. It is split into nonbonded $U^{NB}(\mathbf{r})$ and bonded contributions as follows:

$$U^{Tot}(\mathbf{r}) = U^{NB}(\mathbf{r}) + \sum_{Bends} U^{Bend}(\theta_{ijk}) + \sum_{Dihedrals} U^{Dihedral}(\phi_{ijkl}) + \sum_{Improper\ Dihedrals} U^{Imp}(\phi_{ijkl}^{Imp}) \quad (1)$$

where the sums are over all bends, dihedrals, and improper dihedrals in the system. The contributions of each of these terms, respectively, are calculated as:

$$U^{Bend}(\theta_{ijk}) = \frac{1}{2} k_{\alpha\beta\gamma}^{Bend} (\theta_{ijk} - \theta_{ijk}^0)^2 \quad (2)$$

$$U^{Dihedral}(\phi_{ijkl}) = \sum_n \frac{1}{2} k_{\alpha\beta\gamma\delta, n}^{Dihedral} [1 - \cos(n\phi_{ijkl})] \quad (3)$$

$$U^{Imp}(\phi_{ijkl}^{Imp}) = \frac{1}{2} k_{\alpha\beta\gamma\delta}^{Imp} (\phi_{ijkl}^{Imp})^2 \quad (4)$$

where θ_{ijk} and θ_{ijk}^0 are the instantaneous and natural bending angles for atoms i, j , and k ; ϕ_{ijkl} is the dihedral angle for atoms i, j, k , and l ; and ϕ_{ijkl}^{Imp} is the out-of-plane bending angle for an sp^2

center at atom j . The strength of these interactions is characterized by the corresponding force constants: $k_{\alpha\beta\gamma}^{Bend}$, $k_{\alpha\beta\gamma\delta}^{Dihedral}$, and $k_{\alpha\beta\gamma\delta}^{Imp}$ respectively, where the subscripts $\alpha, \beta, \gamma, \delta$ represent the atom type for atoms i, j, k , and l respectively. There are no bond energy terms due to the fact that bonds are always constrained at a bond specific fixed distance.

The nonbonded energy [$U^{NB}(\mathbf{r})$] is generated by summing the two-body repulsion and dispersion energy terms [$U^{RD}(\mathbf{r})$], the energy due to interactions of fixed charges [$U^{Coul}(\mathbf{r})$], and the polarization energy [$U^{Pol}(\mathbf{r})$], arising from the interaction between induced dipoles with both fixed charges and other induced dipoles:

$$U^{NB}(\mathbf{r}) = U^{RD}(\mathbf{r}) + U^{Coul}(\mathbf{r}) + U^{Pol}(\mathbf{r})$$

$$= \sum_{i>j} \left(A_{\alpha\beta} \exp(-B_{\alpha\beta} r_{ij}) - \frac{C_{\alpha\beta}}{r_{ij}^6} + D \left(\frac{12}{B_{\alpha\beta} r_{ij}} \right)^{12} \right) + \sum_{i>j} \left(\frac{q_i q_j}{4\pi\epsilon_0 r_{ij}} \right) - \frac{1}{2} \sum_i \bar{\mu}_i \cdot \bar{E}_i^0 \quad (5)$$

where $\bar{\mu}_i = \alpha_i \bar{E}_i^{Tot}$ is an induced dipole at force center i , α_i is the isotropic atomic polarizability, \bar{E}_i^{Tot} is the total electrostatic field at the atomic site i due to permanent charges q_j and induced dipoles $\bar{\mu}_j$, ϵ_0 is the dielectric permittivity of vacuum, \bar{E}_i^0 is the electric field due to fixed charges only, $A_{\alpha\beta}$ and $B_{\alpha\beta}$ are the repulsion parameters and $C_{\alpha\beta}$ the dispersion parameter for interaction between atoms i and j with atom types α and β . The term $D \left(12/B_{\alpha\beta} r_{ij} \right)^{12}$, with $D = 5 \times 10^{-5}$ kcal/mol for all pair interactions not involving a lone pair force center, is essentially zero at typical nonbonded atomic separations, but becomes the dominant term at $r_{ij} < 1$ Å, ensuring that $U^{RD}(\mathbf{r})$ is repulsive at distances much smaller than the size of an atom.

Intramolecular nonbonded interactions are included for atoms separated by three or more covalent bonds. We have utilized Thole screening¹⁸ ($a_T = 0.2$), which locally “smears” induced dipoles

over a short spatial range, in order to prevent the so-called “polarization catastrophe” from occurring. Additionally, a reduction by 0.8 is applied to intramolecular interactions between an induced dipole and a partial charge separated by three bonds. Finally, for heteroatom interactions, the modified Waldman-Hagler combining rules were used:

$$\begin{aligned} A_{ij} &= \sqrt{A_{ii}A_{jj}} \frac{B_{ij}^6}{B_{ii}^3 B_{jj}^3} \\ B_{ij} &= \left(\frac{2}{B_{ii}^{-6} + B_{jj}^{-6}} \right)^{1/6} \\ C_{ij} &= \sqrt{C_{ii}C_{jj}} \end{aligned} \quad (6)$$

These combining rules have been successfully used by us for simulations of liquids, polymers, electrolytes, and ionic liquids¹². A , B , and C parameters can be expressed in terms of potential well depth ϵ , the interatomic separation at the minimum R^* , and the steepness parameter λ as given by eq. 7-9:

$$A = 6\epsilon(\exp \lambda)/(\lambda - 6) \quad (7)$$

$$B = \lambda/R^* \quad (8)$$

$$C = \epsilon\lambda(R^*)^6/(\lambda - 6) \quad (9)$$

Partial Atomic Charges. Partial atomic charges are based on the electrostatic potentials of the gas phase molecules calculated on a grid of evenly spaced points ($\sim 10^5$ points per molecule) around the lowest energy gas-phase conformations, with a small weighting also given to the dipole moment ($\vec{\mu}_i$) of the molecule. Cationic and neutral molecular species were based on quantum results calculated at the MP2/aug-cc-pvDz level, while anionic species were calculated at the MP2/cc-pvTz level, with charges assigned in the QC results via the CHelpG charge distribution methodology.¹⁹ Charge-bond increments are used to calculate partial atomic charges,

where the value (q_i) of the partial charge positioned on atom i is calculated as the sum of all charge-bond increments that involve atom i :

$$q_i = \sum_{j=1}^{N_{Bond}} \delta_{ij} \quad (10)$$

with δ_{ij} the charge-bond increment connecting an atom of type i to an atom of type j . The set of charge-bond increments for the overall molecule is determined by minimizing the objective function:

$$\chi^2(\vec{\delta}) = \sum_{i=1}^M \left[\sum_{j=1}^{N_{Grid}} \frac{\omega^\phi}{N_{Grid}} \left(\phi_{ij}^{QC} - \phi_{ij}^{FF}(\vec{\delta}) \right)^2 + \omega^{\vec{\mu}} \left(\vec{\mu}_i^{QC} - \vec{\mu}_i^{FF}(\vec{\delta}) \right)^2 \right] \quad (11)$$

where ϕ_{ij}^{QC} and ϕ_{ij}^{FF} are the electrostatic potential for the i th molecule (or complex) at the j th grid point from QC and the developed force field (FF) respectively, $\vec{\mu}_i^{QC}$ and $\vec{\mu}_i^{FF}$ are the dipole moments, and ω^ϕ and $\omega^{\vec{\mu}}$ are the relative weights for fitting the electrostatic potential and the dipole moments respectively. The electrostatic potential weighting was set to 1.0, with the dipole weighting set to 0.1 for all systems. All points within 1.8 Å of an oxygen atom, 1.5 Å of a hydrogen atom, 2.5 Å of a carbon atom, or 2 Å of a nitrogen atom or further from any atom than 4 Å were excluded from the fitting. For the dicyanamide, nitrate, and azide anions, this process is sufficient to yield a good quality approximation of the electrostatic field due to the molecules. However, for all the hydrazinium cations and the 5-Azidotetrazolate, fitting charge increments only to the explicit atoms in the molecule yielded unsatisfactory results in terms of accurate reproduction of the molecular electrostatic field. In both cases, the solution was to add explicit

off-atom force centers to act as additional degrees of freedom for the charge fitting routine in order to improve the electrostatic potential fit. We therefore add dummy force centers to represent “lone pairs”, with the general approach utilized explained in detail elsewhere.^{20,21} The extended charge center is non-polarizable and has zero mass, contributing only to electrostatic non-bonded interactions via acting as a static partial charge. The electrostatic force induced on the dummy force center is distributed to its attached tri-atomic basis using the chain rule.²²

The importance of including the lone pairs for accurate reproduction of the local electrostatic field of the hydrazinium cations is demonstrated in Figure 2. When the explicit lone-pairs are foregone, the potential near the NH_2 group opposite the positively charged nitrogen is smooth, as shown in Fig. 2a. The quantum chemistry, on the other hand, shows a marked depression in local field (which shows up as a “well” in a constant potential isosurface as plotted in figure 2) in a position which is commensurate with the location one would expect from a lone pair in a tetrahedral configuration attached to the nitrogen in the NH_2 group. In Fig. 2b, we present a comparison of the electrostatic potential surfaces for our hydrazinium cation with the addition of two dummy force centers. With the addition of the lone pair force centers, the simulation electrostatic field becomes far better at approximating the quantum chemistry potential, approximating the potential “well” at a constant electrostatic potential with the same value as depicted in Fig. 2a quite well. It should be noted that the protruding “finger” of quantum potential isosurface that extends further toward the nitrogen in Fig. 2b is due to the fact that the range of the QC surface actually impinges on the excluded radius (2 \AA) of the nitrogen atom in the partial charge calculation (placing it well into the repulsive core of the nitrogen atom). In the force field, the grid points closer than 2.0 \AA to the nitrogen were excluded from the fit and are therefore not shown in Figure 2b.

Introduction of the lone pairs to the NH_2 group has a substantial effect on the overall quality of the electrostatic potential fit in quantitative terms, with the best fit obtained without lone pairs

yielding approximately 1.49, 1.23, and 0.98 kcal/mol mean square deviation observed for N_2H_5^+ , $(\text{CH}_3)\text{N}_2\text{H}_4^+$, and $(\text{CH}_3)_2\text{N}_2\text{H}_3^+$. With the addition of both lone pair force centers, those values reduce to 0.77, 0.77, and 0.78 kcal/mol, respectively. Interestingly, if we simply add the single (outward) lone pair in the direction of the observed QC “well” and calculate the charge fit, the results are only marginally better than for no lone pairs. This resulting necessity of an internally charged “phantom” lone pair is similar to the significantly improved charge fit which occurs with a non-intuitively placed extended force center in the TIP4P water model.²³

In the 5-Azidotetrazolate anion as well, lone pairs significantly improve the reproduction of the electrostatic field near the molecule. Here, however, the difference is subtler in nature. Initial predictions of the electrostatic field around the tetrazolate ring without the lone pair force centers yields a field which is too round in character, as demonstrated by the red surface in Figure 3. Due to the aromatic nature of the nitrogens in the ring (as well as the resonant nature of the azide nitrogen connected to the ring’s single carbon atom) we have added planar lone pairs to all of the ring nitrogens as well as the azide nitrogen connected to the ring carbon. The resultant electrostatic fit to the quantum chemistry is shown by the blue surface in Fig. 3, and can be seen to be generally excellent, with only a small bit of the “cusp” near the azide-carbon bond not well accounted for. For this system, the initial mean square deviation between force field and QC calculations is 3.14 kcal/mol, while the inclusion of the explicit lone pairs drops this value to 1.00 kcal/mol.

We did not fit charges for the cation-anion pairs because proton transfer was found via QC calculation at the MP2/aug-cc-pvDz level of theory for all ion pairs except the $[(\text{CH}_3)_2\text{N}_2\text{H}_3][\text{NO}_3]$ and $[\text{N}_2\text{H}_5][\text{N}(\text{CN})_2]$ systems. In the former exception the nitrate anion and dimethylhydrazinium cation jointly share the proton in the minimum energy configuration, while only in the hydrazinium/dicyanamide system do the cation and anion retain their ionized nature in

the gas phase. For the same reason, we did not validate ability of the force field to reproduce the cation-anion binding energy obtained from quantum chemistry calculations.

For the $[\text{N}_2\text{H}_5][\text{NO}_3]$, we have run further calculations using the polarizable continuum model, calculating $[\text{N}_2\text{H}_5][\text{NO}_3]$ pair interactions within a cavity which is in turn embedded in a continuum model background with the dielectric properties of acetone. In the cavity within acetone, a hydrazine/nitric acid pair at the interaction distances and geometries generated from the isolated gas phase QC calculation undergoes ionization, regenerating the expected $[\text{N}_2\text{H}_5][\text{NO}_3]$ ion pairing.

Atomic Polarizabilities. Isotropic atomic polarizabilities are calculated from both the gas phase molecular dipole moment and explicit binding energy QC calculations between the molecule of interest and a test charge performed at the MP2/aug-cc-pvDZ (MP2/cc-pvTz) level of theory for neutral and cationic (anionic) molecules. Due to the transferable nature of the force field, it is generally only necessary to calculate the polarizability of a specific atom type once for each general chemical environment it occupies, after which this polarizability is used transferably for other atoms in similar chemical environments. This approach has yielded good results for a number of previous investigations.^{12,24,25} Polarization interactions between atoms separated by one or two bonds are assumed to be subsumed within the bond and bend respectively, and are therefore excluded from our calculations.

In this work the practical upshot of this approach is that we have calculated the polarizability of the nitrogen in the neutral hydrazine, and transferred the atomic polarizability to the cationic hydrazinium nitrogen atoms. In combination with the charge fitting outlined previously, this yielded predictions for molecular polarizability of the cations which were within 5% of the QC values, with N_2H_5^+ having a value of 2.48 \AA^3 (QC = 2.53 \AA^3), $(\text{CH}_3)\text{N}_2\text{H}_4^+$ at 4.13 \AA^3 (QC = 4.35 \AA^3), and $(\text{CH}_3)_2\text{N}_2\text{H}_3^+$ showing 5.80 \AA^3 from force field calculations vs. a QC value of 6.00 .

For the anionic species, we fit only the azide and CN_7^- anions, since the $\text{N}(\text{CN})_2^-$ and NO_3^- anions were previously fit.¹² We first fit the polarizability of the azide anion using a teardrop shaped charge path both along and at a 45 degree angle to the principle axis of the molecule, yielding a calculated molecular polarizability of 3.37 \AA^3 for the force field vs. 3.39 \AA^3 for the QC. We then utilized these polarizabilities directly for the azide tail of the CN_7^- molecule, as well as transferring the terminal nitrogen polarizability from the azide to the CN_7^- ring nitrogens since both molecules are comprised of resonant anionic nitrogen atoms. The resultant molecular polarizabilities for the CN_7^- ion predicted by the force field was 8.65 \AA^3 compared to the QC value of 11.35 \AA^3 . Attempts to increase the molecular polarizability to more accurately represent the quantum values provided a dilemma: We could easily increase the value of the polarizability, but only at the expense of the quality of fit of the overall molecular dipole. The as-transferred parameters were found to yield the best fit to the dipole of the overall molecule, yielding under-prediction of the molecular polarizability by ~25%. This level of reduction in the overall molecular polarizability has been found to be necessary in previous simulations that were able to accurately reproduce the crystal structure of the TATB molecular crystal.²⁶ It is noteworthy that TATB also represents a molecular system comprised of resonant ring structures with the presence of strong hydrogen bonding.

Valence and Dihedral Parameters. Bond lengths were constrained for the MD simulations, with values fixed to reproduce those in single-molecule QC calculations at the MP2/aug-cc-pvDz (neutral and cations) and MP2/cc-pvTz (anions) theory level. The QC calculations using triple- ζ basis sets for anions were chosen over the aug-cc-pvDz basis set due to their ability to consistently better represent the bond lengths observed via X-ray measurement of the ionic crystals. The natural bending angles (θ_{ijk}^0) were fit to the optimized QC geometries, with angles in common chemical environments constrained to have the same force field parameters across instances where the angle's central atom is bonded to the same elements, in the same nominal

charge state, in the same or symmetrically equivalent orders (i.e. one set of common angular parameters for the H–N–H angle of the NH₂ group bonded to the “neutral” nitrogen in the hydrazines regardless of methylation state, another set for the cationic hydraziniums where the NH₂ group is bonded to the formally +1 charged nitrogen, with parameters again equal across all three methylated derivatives).

The torsional (dihedral) parameters are fit to energies from MP2/aug-cc-pvDz//MP2/cc-pvTz level scans of the dihedral angle(s) fixed in ten degree increments up to the maximum symmetry-reduced angle, with the remainder of the molecular degrees of freedom allowed to relax. In general, since the torsional description of the chain is intimately linked to the description of the individual bends, we pursued a self-consistent state for the parameterization of both the bending and dihedral angles, with fitting alternating between first one and then the other sets of parameters until the parameters became stable with respect to fitting the complementary set of parameters. We found that achieving this level of stability in the description of the bending and torsional characterization led not only to geometrically consistent descriptions of the isolated molecule, but also to a valence description in which the out-of-plane (improper) torsional contribution was minimal, with the related energetic constant essentially remaining zero. This latter is especially important since the NH₂ group is capable of undergoing inversion at high temperature, which circumvents the full torsional energy in certain systems, and it is therefore important to accurately capture the inversion profile of the improper torsion to ensure proper energetics of the hydrazines and hydraziniums.

Repulsion-Dispersion Parameters. Fitting repulsion-dispersion (R/D) interaction parameters (A,B,C in eq. 6 or ϵ , λ , R^* in eqs. 7-9) is the most challenging and controversial part of force field development since the parameters can be obtained by fitting to a number of different data sets yielding somewhat different potentials. The most often used data for fitting the repulsion dispersion parameters are crystal structures together with sublimation energies, liquid densities,

and heats of vaporization (H^{vap}), vapor-liquid equilibrium data, and gas-phase dimer binding energies obtained from QC calculations. In previous work we have fit the R/D parameters to the density and H^{vap} of nonionic liquids, while the density and dynamic properties were used for IL specific parameters.¹² While this approach has proven to work very well, it is intractable for our current investigation because of the dearth of information concerning dynamic properties of most of the ILs investigated. In general, due to the energetic nature of these compounds, little experimental data is known regarding dynamic properties for the ionic forms of the compounds of interest in the liquid state. Thus, we have fit R/D potentials of the ionic forms via transferring them from the non-ionic precursors, which have in turn been fit primarily based on reproducing the liquid state densities and H^{vap} for clear precursors where available (e.g. the substituted hydrazines) or for an unambiguously functionalized derivative (e.g. 1-Azidobutane for the azide). The sole exception to this was the fitting of the (heavily screened) N^+ homoatomic potential, which has been generated by rescaling the neutral nitrogen R/D potential as discussed previously.¹² For DCA^- and NO_3^- , full parameterizations of good accuracy were available from previous efforts with differing cationic species.^{12,13}

III. Simulation methodology

Simulations in both the crystalline and liquid phases have been carried out utilizing the Lucretius²⁷ molecular simulation package. Periodic boundary conditions were used in all simulations, with covalent bond lengths constrained using the velocity-Verlet form of the SHAKE algorithm.²⁸ The Ewald summation method was used for the treatment of long range electrostatic forces between partial charges, as well as between partial charges and induced atomic isotropic dipoles, while direct induced dipole-induced dipole interactions were calculated only via an iterative realspace summation. The number of reciprocal Ewald vectors was chosen to satisfy the condition $k_i \geq L_i/2\pi$ with k_i the number of Ewald vectors and L_i the total length of the simulation cell along lattice vector i , with $\alpha=0.23$ used for the real-space decay factor. The

number of ion pairs varied from 160 to 384, yielding periodic cell lengths of 30-40 Å, with the particular value between these limits dictated by the size of the crystalline unit cell in most cases. The MD simulations employed a multi-timestep reversible reference system propagator algorithm²⁹, with a time step of 0.5fs for bonds and bend vibrations and a time step of 1.0 fs for dihedral, out-of-plane deformation, repulsion-dispersion (van der Waals) interactions and the real part of Ewald within 7 Å cutoff. A timestep of 2.0 fs was used for all interactions within a 11 Å cutoff including the reciprocal part of Ewald and many-body polarization. A fourth order polynomial tapering function was employed to drive the induced-dipole/induced-dipole interactions to zero at this cutoff, with scaling starting at 10.2 Å.

A combined MD-Monte Carlo (MD-MC) approach^{30,31} was utilized to obtain crystal relaxation at 1 atm pressure and the appropriate temperatures for comparison to experimentally available crystal structures. In all cases, the experimentally derived crystal coordinates were used as a starting configuration for the MD-MC runs. The MD-MC technique consists of two iterating steps: First, a 500fs trajectory segment of canonical ensemble MD simulation (NVT-MD) is performed, followed by a series of 10 attempted changes to the simulation cell shape and volume via isobaric-isothermal rigid molecule Monte Carlo (NPT-MC) moves that consisted of changing cell parameters. The combined NVT-MD and NPT-MC steps comprise a single iteration, with the input state of each iteration coming from the results of the previous iteration. A total of 5000 iterations were performed for each MD-MC run, generating 50000 attempted MC volume changes and 2.5ns of composite trajectory time. All crystal systems were simulated for at least 2 such production runs, yielding a minimum total simulation time of 5 composite nanoseconds. In all cases, the evolution of the lattice vectors and angles were monitored over time to ensure that they have stabilized at representative values for the system being simulated, with simulation calculations taken only from the latter 2ns or more of the simulation after the lattice quantities are stabilized.

IV. Simulations Results and Discussion

Liquid Density and Heat of Vaporization of Neutral Precursors. Comparisons between measured values and MD simulation results for liquid density and heat of vaporization of the neutral hydrazines, as well as the precursor 1-Azidobutane used to parameterize our azide anion, are presented in Table 1. All of the molecules have been investigated at 298K and 1 atm of pressure, with the resulting predictions for both density and H^{vap} being quite accurate. Particular attention has been paid to accurate reproduction of the decreasing trend of H^{vap} with the addition of subsequent methyl groups in the hydrazine system. For the azide group, in addition to fitting well both the density and H^{vap} of 1-Azidobutane, the azide group in anionic form has also recently been found to accurately reproduce densities and dynamic properties in concert with imidazolium-based cations.³²

We have also calculated the density response for the neutral hydrazine molecules as a function of temperature, which are shown in Tables 2. For hydrazine, density parity at room temperature is quite good, but as the system heats the simulated systems expand more quickly than experimental observations. This effect remains modest in the liquid regime, but becomes significant above the boiling point (387 K) of Hydrazine. For the singly methylated molecule, we obtain reasonable density agreement ($\sim 2.5\%$) for the ranges tested, which all reside below the boiling point of the liquid (361 K). Even better agreement between simulation and experiment is seen for UDMH, with simulations up to slightly above the boiling point of 336 K falling within a density variation of $\sim 1.5\%$. The trend of increasing accuracy with increasing methylation of the hydrazine, coupled with the extensive fitting which has been performed for the methyl group employed, indicates a small deviation in the force field fitting for the NH_2 group of hydrazine, which is very quickly and easily mitigated by the presence of the relatively small and apolar methyl group. This in turn implies that in situations where the local environment of the NH_2

group is less than or similarly polarizable as that seen for pure hydrazine, we would expect the repulsion-dispersion level description of the compounds to provide an adequate definition for good reproduction of NH₂ group interactions.

Crystal Lattice Parameters. We have simulated seven test crystals: [Hyd][NO₃],³³ [MeHyd][NO₃],³⁴ [DiMeHyd][NO₃],³⁴ [MeHyd][N₃],¹⁶ [DiMeHyd][N₃],¹⁷ [Hyd][N(CN)₂], and [Hyd][CN₇].¹⁵ For the entire test set simulated, we find generally good agreement between the simulated crystals and those obtained from experimental investigations, as summarized in Table 3. With the exceptions of [Hyd][NO₃] and [MeHyd][N₃], cell volumes vary by less than 3%, with the former deviating by -6% and -7.1%, respectively. Individual lattice vectors obtained from MD simulations show deviations from experiments generally falling in the range of 6% absolute deviation or less, while lattice angles universally deviate by a roughly 2% absolute magnitude or less. Interestingly, removing an extended charge center (lone pair) on the N₂H₅⁺ cation *improves* the reproduction of the [Hyd][NO₃] crystal structure. However, removing the extended charge from the description of the (CH₃)N₂H₄⁺ cation results in an unstable [MeHyd][NO₃] crystal, as shown in Figure 4. One of the important features of the developed force field is its transferability and subsequent applicability over a large range of systems. Therefore, we chose to systematically add the extended charge to all the hydrazium-based cations because it significantly improves the electrostatic potential description despite obtaining a slightly worse description of the [Hyd][NO₃] crystal compared to the one for the model without the extended charge on N₂H₅⁺. In general we have found that the presence of explicit lone pairs (extended charges) is necessary in a number of the crystals to properly dictate the location of the NH₂ group hydrogens, which in turn seems to be necessary for the formation of hydrogen bonds which are a primary component of maintaining crystal cohesion within many of these systems.

For the [Hyd][N(CN)₂], the structural symmetry of the crystal presents a challenge for both the simulation of the system as well as the refinement of the X-Ray data. The final crystal structure is in the *Cmcm* space group, which predicts a symmetric orientation for the hydrazinium cations with a 50% fractional occupancy of the excess cationic proton on each nitrogen of the hydrazinium ion. This is an indicator that the relative orientation of the NH₃⁺ end of the hydrazinium is effectively randomized in the crystal, with neither direction being preferred over the other in a perfect crystal. Since fractional occupancy is a statistical effect due to symmetry considerations, we are forced when simulating to settle upon some finite implementation of the random hydrazinium orientations.

Earlier calculations of the [Hyd][N(CN)₂] crystal structure indicated a *Pnma* structure, whose lattice differs from that of the *Cmcm* structure primarily in the prediction a slightly larger tilt of the N-N hydrazinium axis within the crystal cell, yielding very similar lattice vector magnitudes and unit cell volume. It is from this data which we took the starting point for our simulations. The presence of the skew within the *Pnma* starting point, coupled with the fact that the proton location are primarily predicted from electron density maps and symmetry considerations, leads to unambiguous placement of the protons within the *Pnma* symmetry, compared to the fractional occupancy of the *Cmcm* group. In practical terms, simulation from the *Pnma* space group starting point reflects a systematic choice of excess proton placement coupled with a slight additional skew relative to the correct *Cmcm* starting point.

For experimental comparison, we present lattice parameters from both the initially calculated *Pnma* crystal structure, as well as the final calculation yielding a *Cmcm* crystal, as well as the associated delta's for the simulation with respect to each crystal. In the case of calculating the delta's for the *Cmcm* crystal, the as-provided lattice vectors represented a permuted set of lattice vectors with respect to those simulated (and calculated) for the *Pnma* crystal. For purposes of ease of comparison, we have removed this permutation by transforming the *Cmcm* axes as

follows: $\langle a \rangle_{Cmcm} \approx \langle b \rangle_{Pnma}$, $\langle b \rangle_{Cmcm} \approx \langle c \rangle_{Pnma}$, and $\langle c \rangle_{Cmcm} \approx \langle a \rangle_{Pnma}$. This permutation was verified by visual comparison of the structure file of the *Pnma* crystal with that of the *Cmcm* crystal, and is wholly unambiguous. We compare the simulation with the properly permuted lattice vectors of the *Cmcm* crystal structure in Table 3. Despite the slight deviation in starting conditions, it can be seen that excellent reproduction of the crystal structure is maintained, indicating that the as-simulated *Pnma* crystal is indeed only a slightly perturbed *Cmcm* structure in the simulated system as well as in the experimental system.

Structural Comparisons We have investigated the effect of increasing methylation on the ion correlation structure for the series of crystals utilizing the NO_3^- anion by calculating the relative density amplification of the oxygen of the NO_3 ion near the hydrazinium cations as:

$$\rho' = \rho(x, y, z) / \rho_{bulk} \quad (12)$$

where $\rho(x, y, z)$ represents the local density of the target atom in a cubic sub-volume of approximately 0.1 Å per side. For the hydrazinium cations, we define the local coordinate system relative to a basis formed by the position of the two nitrogens and the “outward” lone pair force center constant (where the “outward” lone pair is that which simultaneously has a larger than 90° angle with each of the NH_2 N—H bonds as well as the N—N bond). For notational convenience, it will also be of use to define the “top” of the molecule as the half of space which contains the aforementioned “outward” pair and is bisected by a plane embedding the N—N bond, with normal perpendicular to the N—N bond and residing in the plane that embeds both the N—N and N—“outward” Lp bond.

We begin by investigating the differences in the hydrogen bonding structure seen in the crystalline systems comprised of the N_2H_5^+ cation with all of the available anions for the

hydrazinium: NO_3^- , CN_7^- , and $\text{N}(\text{CN})_2^-$. Figure 5 presents graphs of the 3D density isosurfaces defined in Eqn. 12 with $\rho' = 10$, with the differing surface colors representing the negatively charged atomic species for their associated anions (red = O in NO_3^- , blue = N in $\text{N}(\text{CN})_2^-$, yellow = N in CN_7^-), with differing brightnesses qualitatively denoting the relative charge magnitude (brighter is more negative). Thus, there is a single red for all the O in NO_3^- since they are charge equivalent ($q \approx -0.66e$), the lighter blue represents the terminal nitrogens in $\text{N}(\text{CN})_2^-$ ($q \approx -0.68e$) while the dark blue represents the central nitrogen ($q \approx -0.62e$), and there are three shades of gold representing the terminal azide nitrogen (bright, $q \approx -0.36e$), the bonded azide nitrogen (medium, $q \approx -0.28e$), and the 2,3 ring nitrogens (dark, $q \approx -0.25e$). We first looked for areas demonstrating similar hydrogen bonding across all three species, rationalizing that these would represent the primary binding sites which drive the crystalline interactions. In order to more clearly see just these specific locations, Figure 5a presents the density isosurfaces for just the shared isosurface locations, with all additional density isosurfaces removed. The overwhelming importance of strong hydrogen bonding is demonstrated in Figure 5a, as all but one of the sites highlighted by the requirement of concomittant bonding across all three anion species directly relate to interactions between the anions and the hydrogens of the N_2H_5^+ molecule. It should be noted that the depiction of the centralized N_2H_5^+ ion is provided to help anchor the reference of the surrounding density isosurfaces. In reality, the NH_3 group including the positively charged nitrogen is at least partially mobile (leading to the production of charge binding *surfaces* rather than *points*) for the NO_3^- and CN_7^- anions, while simulation data suggests that the $[\text{N}_2\text{H}_5][\text{N}(\text{CN})_2]$ crystal the NH_3 group is able to fully sample it's conformational rotation in the simulated crystal. Whether this is a mis-prediction of the force-field or represents an increased inherent mobility of this group due to intrinsic differences with the interaction of the hydrogens and $\text{N}(\text{CN})_2^-$ when compared to the other anions is not clearly understood.

Figures 5b-d present a number of different viewpoints on the anion binding with the same value of ρ' , with the principal binding sites of Figure 5a left solidly colored, while ancillary binding sites are left transparent. In this case, we believe all of the transparent sites (some of which show correspondence between differing anions, but none of which present correspondence in a singularly predictable fashion between any two anions) represent the effective binding due to steric and packing constraints. These sites represent the inevitable minimization of energy subject to the constraints of intramolecular connectivity and steric intermolecular forces in conjunction with the electrostatic and repulsion/dispersion interactions between nearby species.

While it is difficult to tell just from this type of analysis what the overall relative contributions of any specific interactions are, we believe the principle interactions highlighted in Xa and arising from strong hydrogen bonding are the most fundamental in determining the crystal structure. As further proof of this, we consider the cases of both the $(\text{CH}_3)\text{N}_2\text{H}_4^+$ and $(\text{CH}_3)_2\text{N}_2\text{H}_3^+$ cations, where we have two crystals for each with the nitrate and azide counter-ions. In neither case are we able to provide graphs such as those shown in Fig. 5, because for each of these crystals one of the two crystalline forms stabilizes in a manner which includes a conformational state which perturbs the torsional state of the methylated nitrogen from its lowest energy state ($[(\text{CH}_3)\text{N}_2\text{H}_4][\text{N}_3]$ and $[(\text{CH}_3)_2\text{N}_2\text{H}_3][\text{NO}_3]$ for the methylated and dimethylated cation, respectively). The freezing in of a higher conformational energy state to allow more facile hydrogen bonding is indicative of the overall importance of the hydrogen bonding interaction in stabilizing the crystalline system. Given the importance of the hydrogen bonding in these systems, we have also investigated the relative effect that methylation has upon the hydrogen bonding by looking at the structural correlations in the nitrate containing crystals.

To understand the effect of progressive methylation, we investigate correlation isosurfaces for the nitrate bearing crystals by examining relative density amplification of the nitrate oxygens at a level 20 times that of the bulk concentration. In the $[\text{N}_2\text{H}_5][\text{NO}_3]$ system shown in Fig. 6a, there

is ample evidence of strong association between the oxygen and hydrogens, with the positions near the triply hydrogenated end of the N_2H_5^+ cation coordinating an oxygen at the face of the pyramidal base formed by the three hydrogens, as well as showing a tendency to coordinate individually to these hydrogens in the roughly triangular series of “double” density regions located commensurate with the position of these highly charged hydrogens. Of particular interest is the fact that the bottom portion of these “doubled” regions actually shift toward the NH_2 end of the molecule as they descend to take advantage of the extra coordination provided by the hydrogens on the NH_2 , despite the fact that the NH_2 hydrogens also coordinate with another area directly below. Finally, on the upper portion of the NH_2 end of the ion a somewhat complex coordination pattern emerges, presumably due to the necessity to gain some coordination energy above the nitrogen while avoiding the electronegative “well” discussed previously.

When the N_2H_5^+ cation is methylated to form the $(\text{CH}_3)\text{N}_2\text{H}_4^+$ cation, the resultant coordination becomes more centralized due to the steric interference brought about by the presence of the methyl group (Fig. 6b). In this and the following $(\text{CH}_3)_2\text{N}_2\text{H}_3^+$ (Fig. 6c) graphic, it's important to remember that the N^+ group has a symmetric isomer mirrored across the plane which includes the $\text{N}-\text{N}$ bond and bisects the $\text{H}-\text{N}-\text{H}$ angle of the NH_2 group, where in both cases the bottom substituted group is constant while the top substituted group has a symmetric parity across this mirror plane. Keeping this in mind, then, it is easy to see that coordination in the $[(\text{CH}_3)\text{N}_2\text{H}_4][\text{NO}_3]$ system occurs with the oxygen interacting with two hydrogens from the methyl group and one from the N^+ substituted hydrogen on the upper half, or the two hydrogens from the N^+ substituted hydrogen and one from the gauche hydrogen on the NH_2 group. The only additional area of high density is near the NH_2 group, situated below the explicit lone pair and above the NH_2 hydrogens, with the same symmetry as the groups near the triply substituted nitrogen.

We have also investigated the difference between the coordination of the liquid and crystalline systems where possible. For $[\text{N}_2\text{H}_5][\text{CN}_7]$ decomposition occurs within the solid phase before melting occurs, while for the $[\text{N}_2\text{H}_5][\text{N}(\text{CN})_2]$ system facile isomerization to guanazole occurs at temperatures well below the melting temperature, leading to the expectation that pure $[\text{N}_2\text{H}_5][\text{N}(\text{CN})_2]$ liquid is nearly or totally non-existent.³⁵ For $[\text{N}_2\text{H}_5][\text{NO}_3]$, while a liquid phase is known to exist experimentally, we were unable to simulate such a system due to overly strong interactions between the acidic hydrogen atoms attached to the N^+ atom and either the lone pairs on the other end of a neighboring hydrazinium atom, or between the oxygen of the $[\text{NO}_3]$ ion and the acidic hydrogen attached to the N^+ atom. For the remaining systems involving the $(\text{CH}_3)\text{N}_2\text{H}_4^+$ and $(\text{CH}_3)_2\text{N}_2\text{H}_3^+$ cations in concert with the NO_3^- and N_3^- anions, we compare the structure from the crystal at experimentally observed temperatures with that of a liquid which is uniformly held at 353K across all liquid samples. The liquid simulation was run for a minimum of 6ns, and the local density enhancement of ion correlations calculated as above.

Figure 7 presents a comparison of the observed ion correlation structures for the liquid and crystalline systems for the four systems for which liquid data was obtainable. For both $[(\text{CH}_3)\text{N}_2\text{H}_4][\text{NO}_3]$ and $[(\text{CH}_3)_2\text{N}_2\text{H}_3][\text{N}_3]$ (Figs. 7a and 7d) the differences between crystal and liquid packing are rather small, with the relaxed steric constraints of the liquid phase allowing the anions to interact primarily through the acidic hydrogens attached directly to the respective nitrogens in the liquid, rather than forcing interaction with the only slightly charged hydrogens of the methyl groups, as occurs in the crystal phase. By comparison, both $[(\text{CH}_3)_2\text{N}_2\text{H}_3][\text{NO}_3]$ and $[(\text{CH}_3)\text{N}_2\text{H}_4][\text{N}_3]$ (Figs. 7b and 7c) show significantly larger differences between the crystal and liquid phases. For both of these cations, in the crystalline phase there is sufficient binding energy due to the proximity of the anions, and the hydrogen bonding which accompanies this proximity, to lead to the stabilization of cationic conformations in the crystal phase which are not the lowest energy conformer. In both cases, the presence of external hydrogen bonds leads to a

conformation in the crystal phase with a methyl group in the *trans* position relative to the upward lone pair of the NH₂ group (represented by the transparently depicted groups in Figs. 7b and 7c), which serves the effect of exposing the acidic hydrogens on the substituted N⁺ atom to attack from anionic groups from all angles, allowing the crystal to stabilize. In the liquid phase, where accommodation of strong steric interactions loses importance, the cations regain their standard low energy conformation with hydrogens, rather than methyl groups, in the *trans* position. This is especially notable in the [(CH₃)N₂H₄][N₃], where, keeping the N⁺-N-Lp basis as constant, the difference in conformation leads to a near total inversion in the spatial location of primary anion association near the N⁺ atom. For both of these systems, the net effect is a far larger localization of anionic counter-charge in the liquid phase compared to the crystalline phase.

Mechanical Properties

We utilize the formalism of Parinello and Rahman,³⁶ which relates the elastic stiffness tensor (C_{ijkl}) to the fluctuations in the elastic strain tensor $\langle \epsilon_{ij} \epsilon_{kl} \rangle$ of the material, to calculate the elastic behavior of our simulated crystals via the observed fluctuations in the lattice vectors from our MD/MC simulations. In the equations that follow, we use a bolded, double-overbarred quantity ($\overline{\overline{\mathbf{A}}}$) to represent a four-dimensional tensor and a bolded, single-overbarred quantity ($\overline{\mathbf{A}}$) to represent a two-dimensional tensor (matrix). A bolded quantity (\mathbf{A}) is a vector, and a non-bolded quantity (A) a scalar. The inner product is represented by $\overline{\overline{\mathbf{A}}} : \overline{\mathbf{B}}$ while an outer product is represented by $\overline{\mathbf{A}} \otimes \overline{\mathbf{B}}$.

In a generic elastic solid, the fundamental stress-strain equations are:³⁷

$$\overline{\overline{\sigma}} = \overline{\overline{C}} : \overline{\overline{\epsilon}} \quad (13)$$

$$\overline{\overline{\epsilon}} = \overline{\overline{S}} : \overline{\overline{\sigma}} \quad (14)$$

where $\bar{\sigma}$ is the stress tensor, $\bar{\epsilon}$ the strain tensor, $\bar{\bar{S}}$ the compliance tensor, and $\bar{\bar{C}}$ the stiffness tensor.

Due to the symmetry of the stress and strain tensors, it is possible to rewrite Eqns. 13 and 14 in a contracted form, utilizing Voigt notation ($x_{11} = x_1, x_{22} = x_2, x_{33} = x_3, x_{23} = x_{32} = x_4, x_{13} = x_{31} = x_5, x_{12} = x_{21} = x_6$). This contracts $\bar{\sigma}$ and $\bar{\epsilon}$ each into a 6-dimensional vector, while $\bar{\bar{S}}$ and $\bar{\bar{C}}$ become the familiar 6x6 matrices normally encountered when investigating elastic constants. Due to ambiguity in the possible definitions of the contracted stress and strain, the contracted stiffness and compliance matrices are not necessarily matrix inverses of one another. However, if one uses the construction of Tsai,³⁸ and defines:

$$\sigma = (\sigma_{11}, \sigma_{22}, \sigma_{33}, \sigma_{23}, \sigma_{13}, \sigma_{12}) \quad (15)$$

$$\epsilon = (\epsilon_{11}, \epsilon_{22}, \epsilon_{33}, 2\epsilon_{23}, 2\epsilon_{13}, 2\epsilon_{12}) \quad (16)$$

the resulting contraction of the compliance and stiffness tensors yield:

$$\begin{aligned} \bar{S}_{V_{ij}V_{kl}} &= \bar{\bar{S}}_{ijkl} \text{ for } \{1 \leq V_{ij} \leq 3 \text{ and } 1 \leq V_{kl} \leq 3\} \\ \bar{S}_{V_{ij}V_{kl}} &= 2\bar{\bar{S}}_{ijkl} \text{ for } \{1 \leq V_{ij} \leq 3 \text{ and } 4 \leq V_{kl} \leq 6\} \text{ or } \{4 \leq V_{ij} \leq 6 \text{ and } 1 \leq V_{kl} \leq 3\} \\ \bar{S}_{V_{ij}V_{kl}} &= 4\bar{\bar{S}}_{ijkl} \text{ for } \{4 \leq V_{ij} \leq 6 \text{ and } 4 \leq V_{kl} \leq 6\} \end{aligned} \quad (17)$$

$$\bar{C}_{V_{ij}V_{kl}} = \bar{\bar{C}}_{ijkl} \text{ for all } V_{ij}, V_{kl} \quad (18)$$

Under these definitions, the contracted matrices \bar{C} and \bar{S} are simple matrix inverses of each other.

Calculation of elastic constants may then proceed by noting that:³⁶

$$\bar{\bar{S}} = \langle \bar{\epsilon} \otimes \bar{\epsilon} \rangle \frac{\langle V \rangle}{k_B T} \quad (19)$$

where the angle brackets denote system averages, $\bar{\bar{S}}$ is the compliance, V is the volume of the simulated cell at temperature T , k_B is Boltzmann's constant, and $\bar{\epsilon}$ is the strain, given by:

$$\bar{\varepsilon} = \frac{1}{2} \left(\bar{\mathbf{h}}_0^{-1} \bar{\mathbf{G}} \bar{\mathbf{h}}_0^{-1} - \mathbf{1} \right) \quad (20)$$

with $\bar{\mathbf{h}}_0$ is the reference state of the system, and $\bar{\mathbf{G}} = \bar{\mathbf{h}} \bar{\mathbf{h}}$ is the metric tensor of the current (instantaneous) system state. Here, a prime (') represents a matrix transpose. We take $\bar{\mathbf{h}}_0$ to be equivalent to the average over the entire set of sampled cells.

We have performed these calculations on all 7 of our simulated crystals, with the results summarized in Table 4 for the principal compression (C_{11} , C_{22} , C_{33}) and shear (C_{44} , C_{55} , C_{66}) coefficients. Since simulations occurred at different temperatures, a direct comparison amongst the entirety of the data is somewhat problematic. The two significant outliers for temperature are the $[\text{N}_2\text{H}_5][\text{NO}_3]$ system at 120K and the $[\text{N}_2\text{H}_5][\text{CN}_7]$ system at 100K. The remainder of the systems fall at either 173K or 200K, both of which are close enough relative to the other to expect qualitative trends to be accurate. In addition, it is reasonable to expect that the experimental conditions for the unambiguous determination of crystal structure represents a rough regime of “normal” solid handling conditions which might be representative of the behavior of the crystalline systems in actual utilization. Under the second assumption, we can therefore qualitatively compare the stiffness response of the crystals in order to look for broad general trends in mechanical behavior. For the compression stiffness, we find $[\text{N}_2\text{H}_5][\text{CN}_7] \approx [\text{N}_2\text{H}_5][\text{N}(\text{CN})_2] > [\text{N}_2\text{H}_5][\text{NO}_3] > [(\text{CH}_3)\text{N}_2\text{H}_4][\text{NO}_3] \approx [(\text{CH}_3)\text{N}_2\text{H}_4][\text{N}_3] > [(\text{CH}_3)_2\text{N}_2\text{H}_3][\text{NO}_3] \approx [(\text{CH}_3)_2\text{N}_2\text{H}_3][\text{N}_3]$.

For shear stiffness the relations are more complex. In all cases the shear stiffness is smaller than the compression stiffness, with relative compressive to shear stiffness ratios roughly ranging from 2 to 10, depending on the system and direction. The size of the anion and its ability to form a hydrogen bonding network seems to correlate well with the shear stiffness of ionic crystals. For example, $[(\text{CH}_3)_2\text{N}_2\text{H}_3][\text{N}_3]$ with the smallest anion and the least number of hydrogen bonds per ion pair (or per volume) has the lowest stiffness, replacing a methyl group with the hydrogen

$((\text{CH}_3)_2\text{N}_2\text{H}_3^+ \rightarrow (\text{CH}_3)\text{N}_2\text{H}_4^+)$ increases the number of hydrogen bonds per ion pair and increases the stiffness. This trend is clearly observed for the $[\text{N}_2\text{H}_5][\text{NO}_3] > [(\text{CH}_3)\text{N}_2\text{H}_4][\text{NO}_3] > [(\text{CH}_3)_2\text{N}_2\text{H}_5][\text{NO}_3]$ ionic crystals. Increasing the size of anion from N_3^- to NO_3^- , $\text{N}(\text{CN})_2^-$ and CN_7^- for the $(\text{CH}_3)\text{N}_2\text{H}_4^+$ -based ionic crystals generally results in a larger shear stiffness for the larger anions, with the most anisotropic anion CN_7^- yielding the most anisotropic shear stiffness matrix. When comparing the crystals involving $[\text{NO}_3]$ and $[\text{N}_3]$, it is interesting to note that while both anions produce similar compression strengths, there is a substantial difference between their shear strengths, perhaps due to the different shape of the planar $(\text{NO}_3)^-$ group and the linear $(\text{N}_3)^-$.

V. Conclusions

Utilizing a many-body polarizable formulation with explicit lone pairs, we have parameterized a transferrable, consistent force field to represent the hydrazinium cation and its mono-methyl and unsymmetrically dimethylated derivatives in conjunction with N_3^- , NO_3^- , $\text{N}(\text{CN})_2^-$ and CN_7^- anion. We have simulated seven hydrazinium-based crystals across four differing anionic species, with most predictions showing excellent volumetric parity with experiment, on a range of $\sim 2.5\%$ or less, with individual lattice vector deviation of $\sim 1\text{-}6\%$. For the $[\text{N}_2\text{H}_5][\text{NO}_3]$ crystal volumetric deviation is $\sim 6\%$, and for the $[(\text{CH}_3)\text{N}_2\text{H}_4][\text{N}_3]$ crystal $\sim 7\%$, with individual lattice vectors in the $1\text{--}7\%$ range. Of particular interest in the case of the cations is the necessity of including lone pairs to accurately reproduce the local electrostatic field of these ions near the NH_2 group. While lone pair inclusion is relatively standard for both anions and certain neutral molecules, the necessity of their presence on a cationic species is noteworthy. We have also performed liquid state simulations of the neutral hydrazines, as well as the $[\text{NO}_3]$ and $[\text{N}_3]$ based ionic salts. Comparison of the hydrazines shows excellent reproduction of both density and heat of vaporization at room temperature, with density reproduction drifting for the pure hydrazine at elevated temperatures, while predictions for $[\text{MH}]$ and $[\text{UDMH}]$ remain stable.

In ion pair QC calculations at the MP2//cc-pvTz theory level, $[\text{N}_2\text{H}_5][\text{NO}_3]$, $[\text{N}_2\text{H}_5][\text{CN}_7]$, $[(\text{CH}_3)\text{N}_2\text{H}_4][\text{NO}_3]$, $[(\text{CH}_3)\text{N}_2\text{H}_4][\text{N}_3]$, and $[(\text{CH}_3)_2\text{N}_2\text{H}_4][\text{N}_3]$ all show an energetic ground state for each pair with the (cation) anion (de)protonated in the isolated gas phase. For the $[\text{N}_2\text{H}_5][\text{NO}_3]$ pair calculation, we have also done QC in a polarizable continuum, noting that placing the de-ionized pair into a polarizable continuum leads to re-ionization of the constituent neutral molecules. We believe this is indicative of the fact that while *isolated* ion pairs are unstable, bulk phase ionic liquids are effectively stabilized in the ionic state due to the dielectric medium of the surrounding ionic liquid.

It is noteworthy that of the seven crystals we simulate, we see the largest deviation in those that have the smallest anions. Furthermore, the quality of prediction seems to systematically increase with increasing methylation of the hydrazinium cations. Coupled with the above discussions of results in the QC calculations, and noting that we parameterize the charge and polarizability each from the *isolated* gas phase, we believe it may be likely that overly strong charge and/or polarization interactions with respect to the acidic hydrogens on the N^+ atoms are responsible for the undesirable force field behavior. As the molecular structures inherently begin to further screen these interactions (either through increased methylation of the cation or increasing anion size, both of which impedes close approach to the acidic hydrogens in the bulk), the undesirable behavior goes away. This would be consistent with the observation that $[(\text{CH}_3)\text{N}_2\text{H}_4][\text{NO}_3]$ yields better results than $[(\text{CH}_3)\text{N}_2\text{H}_4][\text{N}_3]$, since the N_3^- anion is smaller than the NO_3^- anion and thus more able to attack the hydrogens near the methyl group of $(\text{CH}_3)\text{N}_2\text{H}_4^+$, as well as the better quality results of $[(\text{CH}_3)_2\text{N}_2\text{H}_3][\text{N}_3]$ over $[(\text{CH}_3)\text{N}_2\text{H}_4][\text{N}_3]$ and $[(\text{CH}_3)\text{N}_2\text{H}_4][\text{NO}_3]$ over $[\text{N}_2\text{H}_5][\text{NO}_3]$.

Investigation of anion bonding similarities with a common N_2H_5^+ across three differing crystals demonstrates the importance of hydrogen bonding in stabilizing the various crystals. We found significant differences between hydrazinium cation coordination by anions in the crystal

and liquid phase indicating that the liquid structure should be inferred from the crystal structure with caution. Structural features such as the hydrogen bonding network and ion sizes and shapes were correlated with the shear stiffness matrix of ionic crystals calculations from MD simulations.

Acknowledgements

Financial support of this work was provided by the Air Force Office of Scientific Research (Mike Berman) through contracts FA9550-09-C-0110 and FA9300-06-C-0023. Opinions, interpretations, conclusions, and recommendations are those of the authors and are not necessarily endorsed by the United States Air Force. Computational resources provided through the Department of Defense High Performance Computing Modernization Program (HPCMP) are highly appreciated.

Table 1: Comparison between experimental and simulated densities and enthalpies of vaporization for the neutral hydrazine liquids.

| | N_2H_4 | $(\text{CH}_3)\text{N}_2\text{H}_3$ | $(\text{CH}_3)_2\text{N}_2\text{H}_2$ | 1-Azidobutane |
|------------------------------------|------------------------|-------------------------------------|---------------------------------------|---------------|
| Temp. (K) | 298 | 298 | 298 | 298 |
| Dens. (kg/m^3) | | | | |
| Experiment | 1003.6 | 870 | 791 | 883 |
| Simulation | 1008.7 | 871 | 800 | 881 |
| $\Delta(\%)$ | 0.5 | 0.1 | 1.1 | 0.2 |
| ΔH^{vap} (kcal/Mol) | | | | |
| Experiment | 10.68 | 9.68 | 8.42 | 9.17 |
| Simulation | 10.68 | 9.77 | 8.09 | 9.27 |
| $\Delta(\%)$ | 0.0 | 0.9 | -3.9 | 1.1 |

Table 2: Comparison between predicted and observed densities of the hydrazine liquid force field at elevated temperatures.

| | | | | |
|------------------------------|-------------|------------|------------|--|
| Hydrazine | | | | |
| T (K) | 299.75 | 366.47 | 449.81 | |
| Experiment | 1003 | 940 | 858 | |
| Sim. | 1007 | 916 | 777 | |
| $\Delta(\%)$ | 0.4 | -2.5 | -9.4 | |
| Methylhydrazine | | | | |
| T (K) | 308.15 | 333.15 | 343.15 | |
| Experiment | 858 | 834 | 824 | |
| Sim. | 846 | 815 | 801 | |
| $\Delta(\%)$ | -1.5 | -2.3 | -2.8 | |
| N,N-Dimethylhydrazine | | | | |
| T (K) | 273.2 | 310.26 | 338.73 | |
| Experiment | 812 | 773 | 742 | |
| Sim. | 827 | 786 | 753 | |
| $\Delta(\%)$ | 1.8 | 1.7 | 1.5 | |

Table 3: Comparison between experimentally observed and simulated crystal structures. Lattice vectors are in Å, lattice angles in degrees, and cell volume in Å³.

| | | | | | | | |
|-------------------|--------------|--------------|---------------|---------------|----------------|---------------|----------------|
| <i>Experiment</i> | 8.445 | 7.042 | 10.075 | 90.000 | 108.321 | 90.000 | 568.741 |
| <i>Simulation</i> | 8.49 | 7.18 | 10.04 | 88.50 | 108.90 | 90.69 | 578.29 |
| $\Delta(\%)$ | 0.5 | 1.9 | -0.3 | -1.7 | 0.5 | 0.8 | 1.7 |

| | | | | | | | |
|--|--------------|--------------|--------------|---------------|---------------|---------------|----------------|
| [N₂H₅][N(CN)₂] | | | | | | | |
| <i>Exp. (Pnma)</i> | 6.581 | 9.000 | 7.497 | 90.000 | 90.000 | 90.000 | 444.033 |
| <i>Exp. (Cmcm)</i> | 6.568 | 8.983 | 7.484 | 90.000 | 90.000 | 90.000 | 441.559 |
| <i>Simulation</i> | 6.82 | 8.89 | 7.31 | 90.06 | 90.03 | 89.88 | 443.62 |
| $\Delta_{Pnma}(\%)$ | 3.7 | -1.2 | -2.5 | 0.1 | 0.0 | -0.1 | -0.1 |
| $\Delta_{Cmcm}(\%)$ | 3.8 | -1.0 | -2.3 | 0.1 | 0.0 | -0.1 | 0.5 |

Table 4. Principal elastic constants (in GPa) for the crystals investigated in this work.

| | $[\text{N}_2\text{H}_5]$ $[\text{NO}_3]$ | $[(\text{CH}_3)\text{N}_2\text{H}_4]$ $[\text{NO}_3]$ | $[(\text{CH}_3)_2\text{N}_2\text{H}_3]$ $[\text{NO}_3]$ | $[\text{N}_2\text{H}_5]$ $[\text{CN}_7]$ | $[(\text{CH}_3)\text{N}_2\text{H}_3]$ $[\text{N}_3]$ | $[(\text{CH}_3)_2\text{N}_2\text{H}_3]$ $[\text{N}_3]$ | $[\text{N}_2\text{H}_5]$ $[\text{DCA}]$ |
|----------|---|--|--|---|---|---|--|
| T | <i>120.0 K</i> | <i>200.0 K</i> | <i>200.0 K</i> | <i>100.0 K</i> | <i>200.0 K</i> | <i>173.0 K</i> | <i>173.0 K</i> |
| C_{11} | 42.70±1.21 | 38.38±0.90 | 19.20±0.60 | 55.71±1.48 | 44.83±0.71 | 23.87±0.72 | 54.00±1.31 |
| C_{22} | 42.88±1.46 | 38.95±0.92 | 18.58±0.49 | 97.73±2.82 | 33.45±0.52 | 15.03±0.54 | 94.38±3.59 |
| C_{33} | 109.12±3.09 | 37.40±0.76 | 11.60±0.37 | 60.39±2.17 | 22.98±0.49 | 19.06±0.84 | 43.95±1.77 |
| C_{44} | 22.49±0.75 | 21.88±0.25 | 6.94±0.27 | 6.19±0.17 | 4.44±0.17 | 2.54±0.07 | 11.18±0.29 |
| C_{55} | 21.13±0.64 | 7.38±0.16 | 6.82±0.20 | 28.83±0.89 | 4.94±0.09 | 2.34±0.06 | 12.56±0.52 |
| C_{66} | 22.33±0.97 | 9.62±0.21 | 4.25±0.14 | 9.90±0.17 | 8.07±0.35 | 3.64±0.13 | 10.37±0.29 |

Figure Captions

Figure 1.

Schematics for the neutral hydrazines (a) used as a basis for the hydrazinium cations (b) as well as for the anions (c) employed in this work.

Figure 2.

Representation of the difference in the shapes of the force field derived (solid) and quantum chemistry calculated (MP2/aug-cc-pvDz, mesh) electrostatic surfaces at 0.125eV for the hydrazinium cation without (a) and with (b) explicit lone pairs. The complete inability of the system without lone-pairs to even qualitatively capture the electrostatic potential well near the tetrahedral position of the NH_2 group is evident, with the force field derived potential surface in part (b) clearly descending toward the lone pairs (represented by yellow spheres).

Figure 3:

Comparison of potential isosurfaces at a value of -0.15eV for the $[\text{CN}_7]$ anion. Quantum chemistry calculations are represented by the green mesh, while those for the forcefield without (red solid) and with (light blue, solid) lone pairs are superimposed. There are 5 planar lone pair force centers: One each on the ring nitrogens, with the 5th attached to the C-N-N bend attaching the tetrazole ring to the azide tail.

Figure 4:

Comparison of individual normalized lattice vector evolution for the [MeHyd][NO₃] crystal system for simulations which include (solid) and ignore (dashed) the effect of explicit lone pair force centers. The predicted lattice vector normalized by the experimental value is plotted for the *a*(green), *b*(blue), and *c*(red) principle lattice directions.

Figure 5:

Ion correlations between the hydrazinium cation and all simulated anions. Density isosurfaces represent local amplification of the density of specific atoms of the anions by a factor of 10 over their expected bulk values: oxygen in NO₃⁻ (red), terminal (light blue) and central (dark blue) nitrogens in N(CN)₂⁻, terminal azide (bright yellow), bonded azide (medium gold), and N3/N4 ring (dark gold) nitrogens in CN₇⁻.

Part (a) presents only the density isosurfaces for locations which are fundamentally similar for all three anions, representing the principle locations of hydrogen bonding, while differing views are shown by (b - side), (c - NH₃ end) and (d – below) with the surfaces of (a) colored opaquely while secondary locations (all at the same relative density) which differ from anion to anion are represented with transparent versions of the appropriate color.

Figure 6:

Ion correlations between the hydrazinium cations and the oxygen in the nitrate anions for (a) hydrazinium nitrate, (b) methylhydrazinium nitrate, and (c) dimethylhydrazinium nitrate. Density isosurfaces represent local amplification of oxygen density that is 20 times greater than the bulk density of oxygen in the crystal.

Figure 7:

Comparison of ion correlations for crystalline and liquid systems for (a) [MeHyd][NO₃], (b)[DiMeHyd][NO₃], (c)[MeHyd][N₃], and (d)[DiMeHyd][N₃]. Crystal correlations are represented by the meshed areas, while liquid correlations by the solid yellow areas. For (b) and (c), the cations undergo conformational changes as the crystal melts, with representative conformations for the crystalline system indicated by transparency in the functional groups which show positional deviation due to the differences in average conformations.

Figures

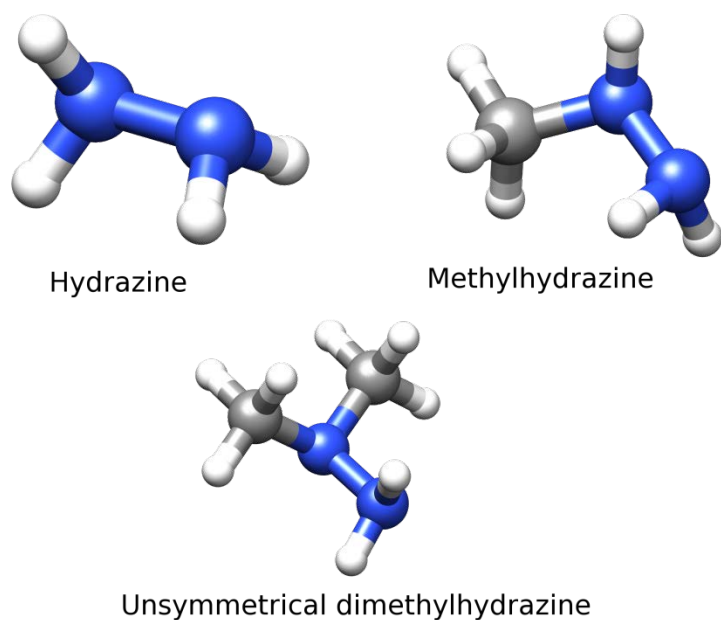
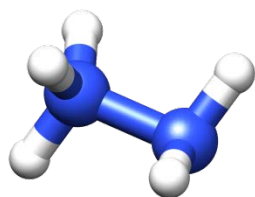
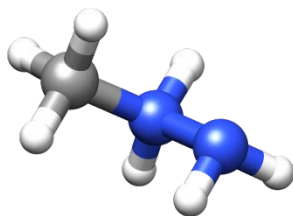


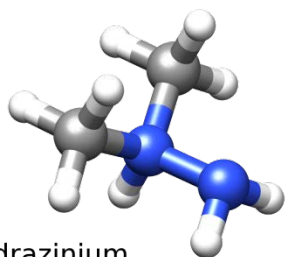
Figure 1a



Hydrazinium

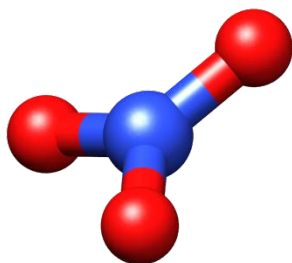


Methylhydrazinium

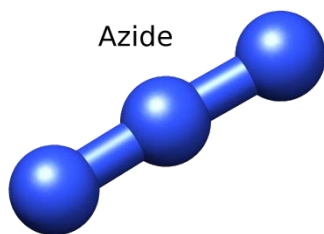


Dimethylhydrazinium

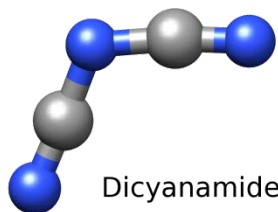
Figure 1b



Nitrate



Azide



Dicyanamide

5-Azidotetrazolate

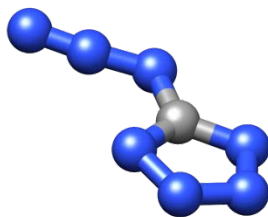


Figure 1c

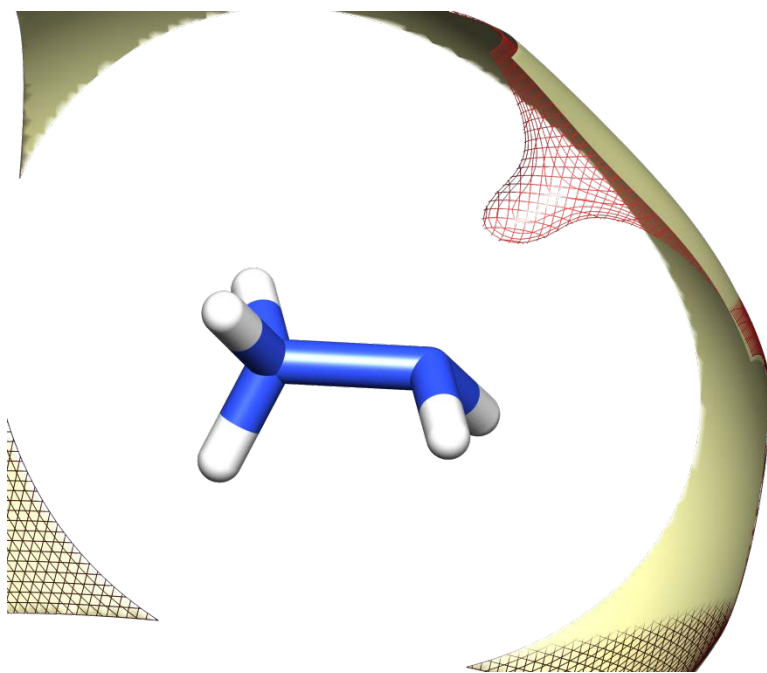


Figure 2a.

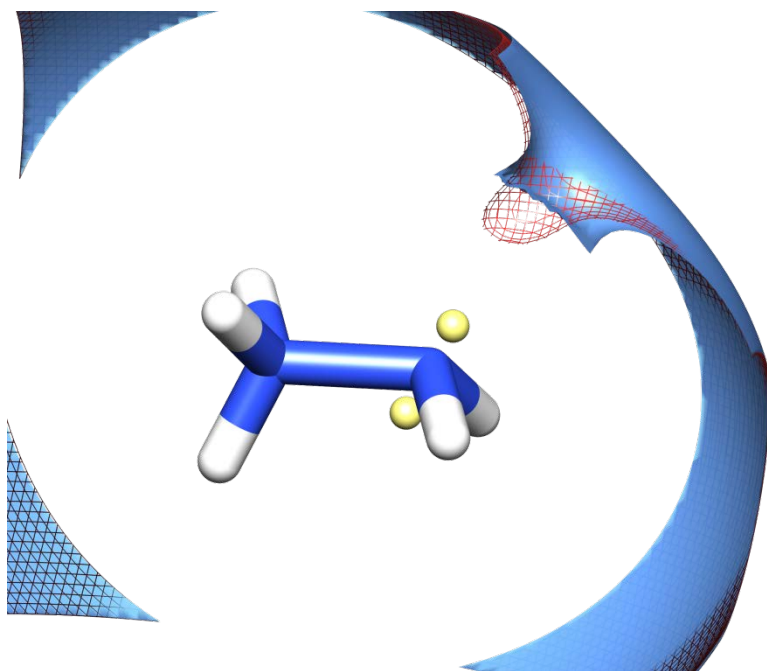


Figure 2b

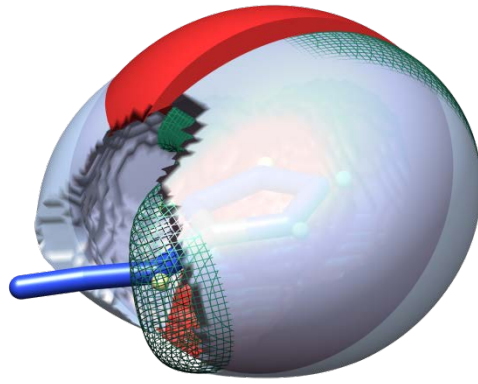


Figure 3

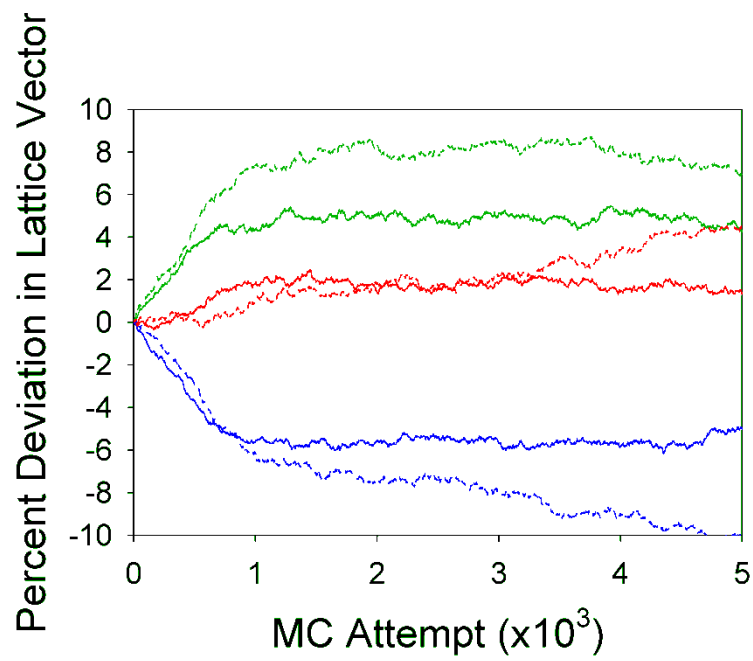


Figure 4

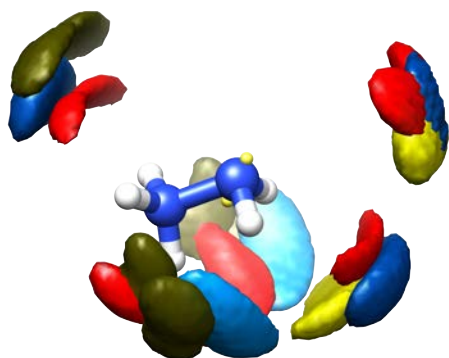


Figure 5a

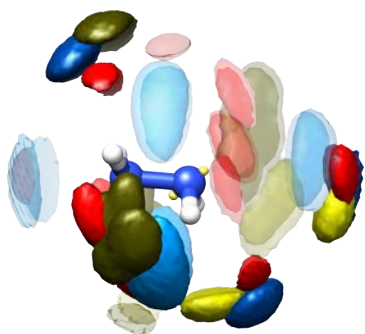


Figure 5b

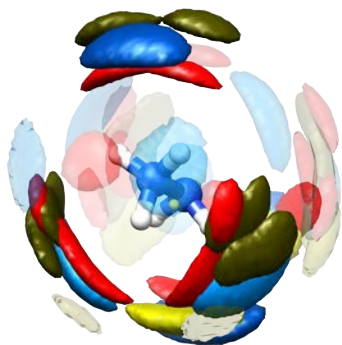


Figure 5c

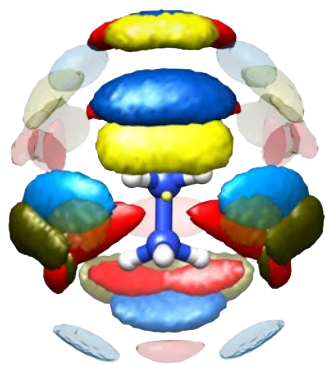


Figure 5d

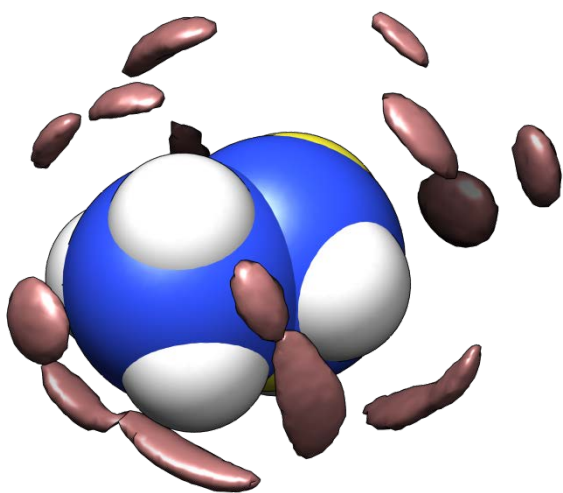


Figure 6a

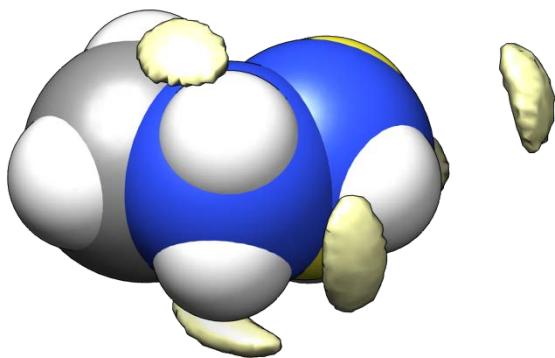


Figure 6b

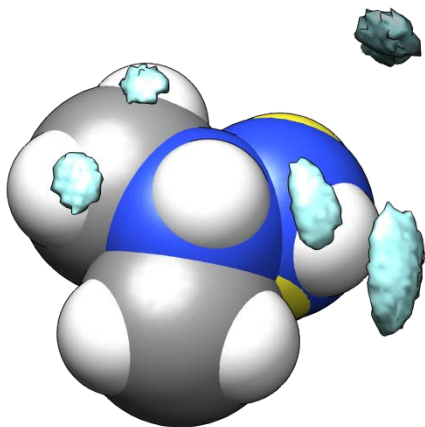


Figure 6c

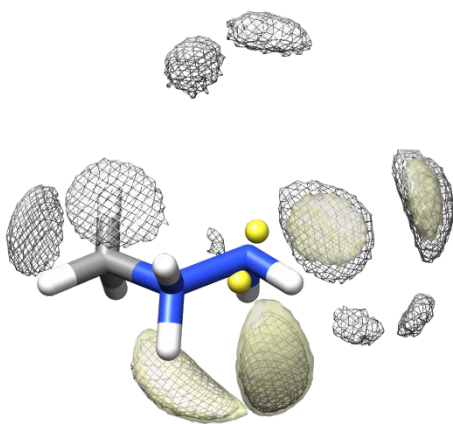


Figure 7a

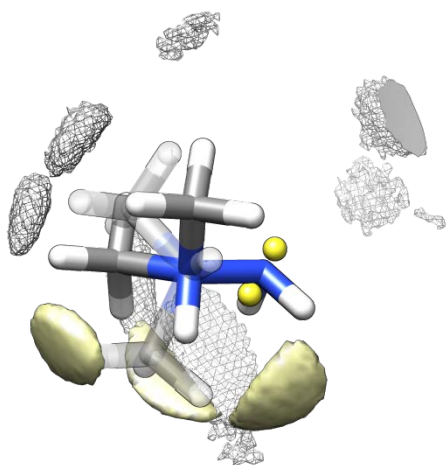


Figure 7b

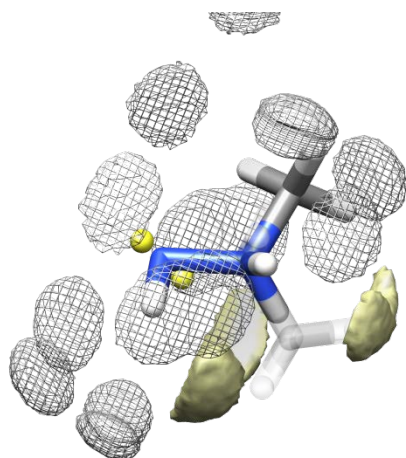


Figure 7c

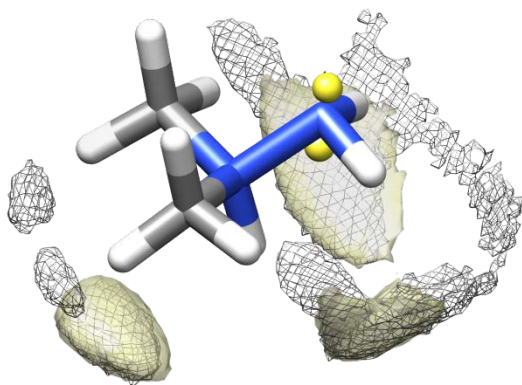


Figure 7d

References

- ¹ E. W. Schmidt, Hydrazine and Its Derivatives: Preparation, Properties, Applications 2nd Ed., John Wiley & Sons, New York (2001).
- ² L.B. Zung, E.A. TKachencko and B.P. Breen, *A Basic Study on the Ignition of Hypergolic Liquid Propellants*, NASA Technical Report No. CR-100387, November, 1968.
- ³ T.W. Price and D.D. Evans, *The Status of Monopropellant Hydrazine Technology*, NASA Technical Report No. CR-92742, February, 1968.
- ⁴ B. Toth, *J. Canc. Res. And Clin. Onc.*, **97**,1432 (1980).
- ⁵ 14. Kinkad, C.C. Haun, E.H. Vernot and J.D. MacEwen, *A Chronic Inhalation Toxicity Study of Monomethylhydrazine*, AFAMRL Technical Report No. TR-85-025, 1985.
- ⁶ S.A. Forsyth, J.M. Pringle, D.R. MacFarlane, *Australian Journ. Chem.*, **57**, 113 (2004).
- ⁷ M. Smiglak, A.Matlen, R.D. Rogers, *Acc. Chem. Res.*, **40**, 1182 (2007).
- ⁸ S. Schneider, T. Hawkins, M. Rosander, G. Vaghjiani, S. Chambreau, G. Drake, *Energy & Fuels*, **22**, 2871 (2008).
- ⁹ S. D. Chambreau, S. Schneider, M. Rosander, T. Hawkins, C. J. Gallegos, M. F. Pastewait, G. L. Vaghjiani, *J. Phys. Chem. A*, **112**, 7816 (2008).
- ¹⁰ S. Schneider, T. Hawkins, M. Rosander, J. Mills, G. Vaghjiani, S. Chambreau, *Inorg. Chem.* **47**, 6082 (2008).
- ¹¹ Y. Zhang, H. Gao, Y. Guo, Y.-H. Joo, J. M. Shreeve, *Chem. Eur. J.* **16**, 3114 (2010).
- ¹² O. Borodin, *J. Phys. Chem. B.*, **113**, 11467 (2009).
- ¹³ J.B. Hooper and O. Borodin, *Phys. Chem. Chem. Phys.*, **12**, 4635 (2010).
- ¹⁴ K. E. Gutowski, B. Gurkan, E. J. Maginn, *Pure Appl. Chem.*, **81**, 1799 (2009).
- ¹⁵ T.M. Klapotke, J. Stierstorfer, *J. Am. Chem. Soc.*, 2009, **131**, 1122.
- ¹⁶ A. Hammerl, G. Holl, K.Hubler, M.Kaiser, T.M. Klapotke and P.Mayer, *Eur. J. Inorg. Chem.*, **2001**, 755 (2001).
- ¹⁷ T.M. Klapotke, H. Noth, H. Schewnk-Kircher, W-H Walther, G. Holl, *Polyhed.* 1999, **18**, 717.
- ¹⁸ B.T. Thole, *Chem. Phys.*, **59**, 341 (1981).
- ¹⁹ C.M. Breneman and K.B. Wiberg, *J. Comp. Chem.*, **11**, 361 (1990).
- ²⁰ O. Borodin and G. D. Smith, *J. Phys. Chem. B*, **113**, 1763 (2009).
- ²¹ G. A. Kaminski, H. A. Stern, B. J. Berne, R. A. Friesner, Y. X. Cao, R. B. Murphy, R. Zhou and T. A. Halgren, *J. Comp. Chem.*, **23**, 1515 (2002).
- ²² K.A. Feenstra, B. Hess, H.J.C. Berendsen, *J. Comp. Chem.*, **20**, 786 (1999).
- ²³ W.L. Jorgensen, J. Chandresekhar, J.D. Madura, R.W. Impey, M.L. Klein, *J. Chem. Phys.*, **79**, 926 (1983).
- ²⁴ J. M. Stout and C. E. Dykstra, *J. Phys. Chem. A*, **102**, 1576 (1998).
- ²⁵ N. E. B. Kassimi and A. J. Thakkar, *Chem. Phys. Lett.* **472**, 232 (2009).
- ²⁶ D. Bedrov, O. Borodin, G. D. Smith, T. D. Sewell, D. M. Dattelbaum and L. L. Stevens, *J. Chem. Phys.*, **131**, 224703 (2009).
- ²⁷ <http://www.eng.utah.edu/~gsmith/lucretius.html>

- ²⁸ B. J. Palmer, *J. Comput. Phys.*, 1993, **104**, 470.
- ²⁹ G. J. Martyna, M. E. Tuckerman, D. J. Tobias, and M. L. Klein, *Mol. Phys.*, **87**, 1117 (1996).
- ³⁰ O. Borodin, G. D. Smith, T. D. Sewell, D. Bedrov, *J. Phys. Chem. B*, **112**, 734 (2008).
- ³¹ T. D. Sewell, R. Menikoff, D. Bedrov, and G. D. Smith, *J. Chem. Phys.*, **119**, 7417 (2003).
- ³² O. Starovoytov, O. Borodin, J. B. Hooper, G. D. Smith, (*in preparation*).
- ³³ M. S. Grigoriev, P. Moisy, C. D. Auwer, I. A. Charushnikova, *Acta Cryst.*, **E61**, i216 (2005).
- ³⁴ O. de Bonn, A. Hammerl, T. M. Klapotke, P. Mayer, H. Piotrowski, H. Zewen, *Z. Anorg. Allg. Chem.*, **627**, 2011 (2001).
- ³⁵ M. B. Frankel, E. A. Burns, J. C. Butler and L. Wilson, *J. Organic Chem.*, **28**, 2428 (1963).
- ³⁶ M. Parrinello and A. Rahman, *J. Chem. Phys.*, **76**, 2662 (1982).
- ³⁷ T. Sewell and C. Bennett, *J. Appl. Phys.*, **88**, 88 (2000).
- ³⁸ S. W. Tsai, *Mechanics of Composite Materials, Part II, Theoretical Aspects*, AFML Technical report No. AFMLTR-66-149, November, 1966.

Supplemental Information

Determination of [N₂H₅][N(CN)₂] Crystal Structure

Experimental. Hydrazinium dicyanamide was prepared according to literature [1]. Single crystals were obtained from methanol solution layered with diethylether.

X-ray Analyses. The single-crystal X-ray diffraction data were collected on a Bruker 3-circle-platform diffractometer equipped with a SMART APEX 2 detector with the χ -axis fixed at 54.74° and using MoK α radiation from a fine-focus tube. The goniometer head, equipped with a nylon Cryoloop and magnetic base, was used to mount the crystals using perfluoropolyether oil. The data collection as well as structure solution and refinement were carried out using standard procedures with the APEX2 V.2.1-4, SMART V.5.622, SAINT 7.24A, SADABS, and SHELXTL software packages and programs.^[2] Crystal data and refinement details of crystals of hydrazinium dicyanamide are given in Table 1.

[1] Frankel, M.B.; Burns, E.A.; Butler, J.C.; Wilson, E.R. *J. Org. Chem.* **1963**, 28, 2428.

[2] APEX2 V.2.1-4, SMART V.5.622, SAINT 7.24A, SADABS, SHELXTL ed.; Bruker-AXS, INC.: Madison, WI USA, 2007.

Table S1 Crystal and structure refinement data for hydrazinium dicyanamide.

| | Hydrazinium dicyanamide |
|--|--|
| Formula | C ₂ H ₅ N ₅ |
| Space group | <i>Cmcm</i> orthorhombic |
| a (Å) | 8.983(4) |
| b (Å) | 7.484(3) |
| c (Å) | 6.568(3) |
| $\alpha, \beta, \gamma(^{\circ})$ | 90 |
| V/Å ³ | 441.5(3) |
| $\rho_{\text{calc.}}/\text{g cm}^{-3}$ | 1.491 |
| Z | 4 |
| Formula weight | 99.11 |
| μ/mm^{-1} | 0.112 |
| Temperature (K) | 173(2) |
| $\lambda(\text{MoK}\alpha)$ | 0.71073 |
| Crystal size | 0.20 x 0.15 x 0.10 |
| Theta range $\theta/^{\circ}$ | 3.54 to 25.34 |
| Index range | $-10 \leq h \leq 10, -8 \leq k \leq 8, -7 \leq l \leq 7$ |
| Reflection collected | 2097 |
| Independent [R(int)]/ | 234 [0.0170] |
| Obs. refl. ([I > 2.0 σ (I)]) | 217 |
| F(000) | 208 |
| GooF | 1.186 |
| R ₁ , wR [I > 2 σ (I)] | 0.0264, 0.0738 |
| R ₁ , wR ₂ (all data) | 0.0282, 0.0750 |
| L.diff. peak/hole eÅ ³ | 0.14 and -0.17 |
| Absorption correct. | multiscan SADABS |
| T _{min} , T _{max} | 0.975, 0.990 |
| Data/restraints/param. | 234/0/30 |
| Refinement method | Full-matrix least squares on F ² |
| $R_1 = \Sigma F_o - F_c /\Sigma F_o $; $R_2 = \{\Sigma[w(F_o ^2 - F_c ^2)^2]/\Sigma(w F_o ^2)\}^{1/2}$ | |

CCDC-xxxxxx contains the supplementary crystallographic data for this paper. These data can be obtained free of charge from the Cambridge Crystallographic Data Centre via http://www.ccdc.cam.ac.uk/data_request/cif.

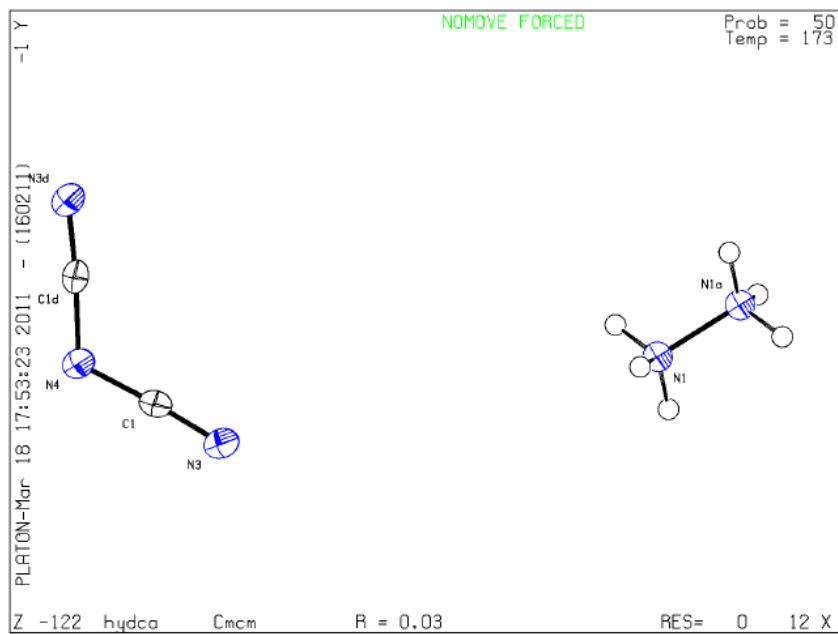


Figure S1. ORTEP diagram showing conformation and atom numbering scheme of hydrazinium dicyanamide.